Understanding Resistance Increase in Composite Inks under Monotonic and Cyclic

Stretching

Qiushi Li, Antonia Antoniou\* and Olivier Pierron\*

G.W. Woodruff School of Mechanical Engineering, Georgia Institute of Technology,

Atlanta, GA, 30318, USA

Emails: antonia.antoniou@me.gatech.edu, olivier.pierron@me.gatech.edu

**ABSTRACT** 

Cyclic degradation in flexible electronic inks remains a key challenge while their deployment in

life critical applications is ongoing. The origin of electrical degradation of a screen-printed

stretchable conductive ink with silver flakes embedded in a polyurethane binder is investigated

under uniaxial monotonic and cyclic stretching, using in-situ confocal microscopy and scanning

electron microscopy (SEM) experiments, for varying ink thickness (1, 2, and 3 layers, each layer

around 8-10 µm) and trace width (0.5, 1, and 2 mm). Cracks form under monotonic stretching, and

the evolution of crack pattern (density, length and width) with applied strain is affected by ink

thickness such that the 3-layer ink exhibit larger normalized resistance but slightly lower resistance

than the 1-layer ink up to strains of 125%. For cyclic stretching, the crack density and length do

not evolve with cycling. However, the cracks widen and deepen, leading to an increase in

resistance with cycling. However, the cracks widen and deepen, leading to an increase in resistance

with cycling. There exists a strong correlation between fatigue life as defined by the number of

cycles until a normalized resistance of 100 is reached, and the strain amplitude. The normalized

resistance increase rate with respect to cycling is also found to scale with strain amplitude. The

rate of change in resistance with cycling decreases with ink thickness and trace width. For practical

applications, thicker (≥25 µm) and wider (≥2 mm) inks should be used to lower resistance

increases with repeated deformation.

**KEYWORDS**: conductive inks, cyclic stretching, failure lifetime, geometrical effects

1. INTRODUCTION

Flexible electronic devices have gained broad interest for their applications in wearable

healthcare monitoring <sup>1-6</sup>, energy storage <sup>7-10</sup>, flexible displays <sup>11-17</sup>, and implantable bioelectronics

<sup>18-19</sup>, to name a few. These devices can integrate rigid or even soft electronic components with

compliant, conformable electric circuits based on stretchable and flexible conductive

interconnects. A major challenge for these flexible devices is maintaining the electrical

performance of the conductive interconnects after repeated deformation, such as repeated

elongation. In wearable devices, such deformations resulting in strains of up to 30-50% are

typically expected <sup>20-21</sup>.

A significant amount of research effort has been made to understand and improve the

electrical reliability of the conductive interconnects. One approach to improving electrical

reliability is by changing the material composition of the interconnect. Thin metal film

interconnects deposited on polymer substrates offer initially high electrical conductivity, but their

usage is limited by the substantial elastic mismatch between the thin metal film and the polymer

substrate, which leads to the loss of conductivity at low strains (typically ~10%) due to cracking

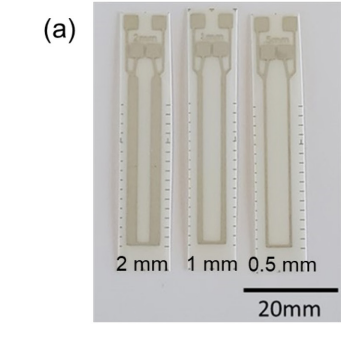
<sup>22-30</sup> and metal fatigue <sup>31-33</sup>. Another class of interconnects is the composite conductive ink consisting of conductive metal flakes embedded in an elastomer binder. <sup>34-43</sup>. These conductive inks have shown promise as electrical interconnects due to their tolerance of higher applied strains when mounted on polymer substrates. The current work studied the PE874 conductive ink provided by DuPont, which is a stretchable ink with silver flakes embedded in a polyurethane binder. The PE874 ink is screen printed onto the TE-11C thermoplastic polyurethane (TPU) substrate.

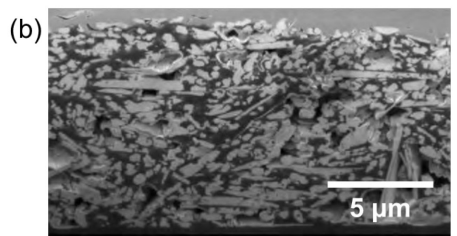
A second approach to improving the electrical reliability of the interconnects involves optimizing the structural configuration of the interconnect lines by changing their sizes, shapes, and structures. Numerous works 44-45 have shown that serpentine shaped interconnects could greatly improve electrical performance under tensile strain compared to straight trace lines and can tolerate cyclic large deformations, due to the maximum local strain being more than an order of magnitude lower than the macroscale applied strains <sup>44, 46</sup>. To characterize the electrical resistance evolution of a conductive ink with both monotonic and cyclic uniaxial elongation for a wide range of strain, specimens with straight trace lines were studied in a number of prior works by Cahn et al. 34, 47-48 due to the relatively uniform deformation and ease of achieving high strains experimentally. The conductive ink's electrical resistance evolution with monotonic strain or cyclic straining, obtained from tests using the straight trace line specimens, can potentially be used to map and predict the resistance evolution in more complex configurations such as serpentines. The width of the interconnect line (trace width) was shown by Sliz et al. 45 to be an important factor in determining the electrical performance of serpentine configured conductive inks; ink thickness could be another important factor. These geometric effects can be investigated efficiently using straight trace line specimen due to the relatively uniform strain distribution.

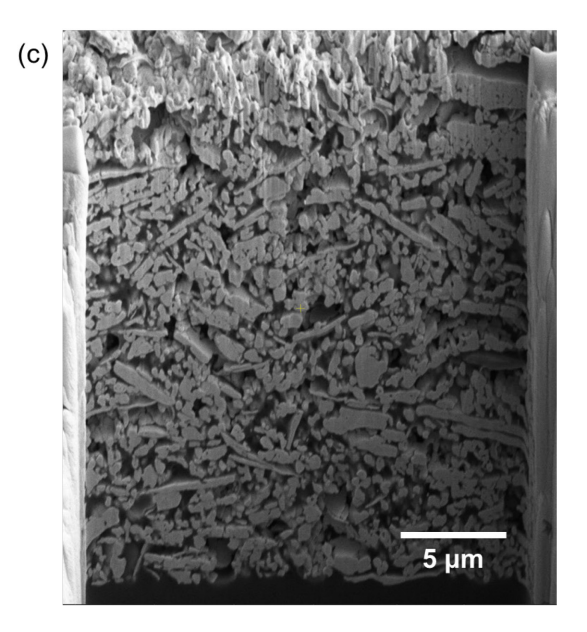
The current work provides a comprehensive investigation of the effects of critical ink geometric and loading conditions on the electrical response of the PE874 ink under uniaxial monotonic and cyclic stretching, as well as a better understanding of the underlying mechanisms behind the electrical resistance increase, thanks to *in-situ* confocal microscope and *in-situ* SEM experiments. The effects of the lengthening, widening, and deepening of the cracks on the electrical resistance evolution with monotonic strain were examined. A series of cyclic stretching (fatigue) tests were performed to investigate the effects of cycling conditions, including the strain amplitude and mean strain during cycling, and geometric conditions, including the ink thickness and trace width, on resistance evolution.

### 2. EXPERIMENTAL AND METHODS

# 2.1. Ink Deposition and Characterization







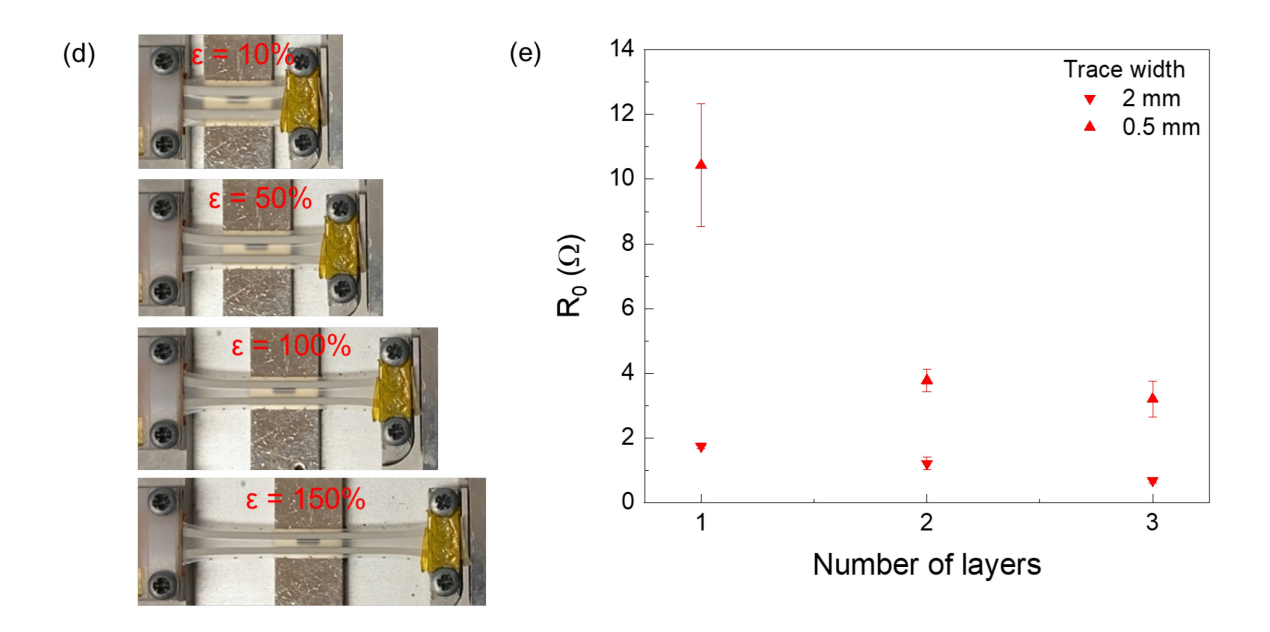


**Figure 1**. (a) Specimens with 2 mm, 1 mm, and 0.5 mm trace widths (left to right); FIB cross-sections for (b) 1-layer and (c) 3-layer ink; (d) Specimen under different tensile strains in the Linkam TST350 testing stage; (e) R<sub>0</sub> for specimens with different number of layers and trace widths in monotonic tests.

The PE 874 conductive ink formulated by DuPont is composed of silver flakes embedded in a polyurethane binder material. The average volume fraction of silver flakes in the ink is about 55% <sup>34</sup>. The PE 874 ink test specimens consist of 1, 2, or 3 layers of the PE 874 ink screen printed onto a thermoplastic polyurethane (TPU) substrate layer in a single pass (for 1-layer specimens) or multiple passes (for 2- and 3-layer specimens). The TPU used for the substrate is the TE-11C from DuPont. The screen-printing process was performed at the DuPont Applications Laboratory with proprietary processes that have been optimized for the ink and substrate. For the first ink layer, a mesh size of 325 threads crossing per inch<sup>2</sup> with wire diameter of 0.9 mil was used. For

the second and third ink layer, a mesh size of 280 threads crossing per inch<sup>2</sup> with wire diameter of 1.2 mil was used. For all cases, mesh angle was 30°. There was a 15 minute drying time after the printing of each ink layer, at 125°C for the first ink layer and 130°C for the subsequent layers. The silver flakes had sizes ranging from several µm to 100s of nm, and occupied 55% of the total volume on average. In addition, there was a large amount of voids in the ink microstructure, with sizes also ranging from several µm to 100s of nm and occupying 17% of the total volume on average. The ink is printed in U-shaped, double trace lines with 2 mm, 1 mm, or 0.5 mm trace width (see Figure 1(a)). The four pads in the print pattern were designed for four-point electrical resistance probes. The average thicknesses of the 1, 2, and 3 ink layers measured by DuPont are 10 µm, 20 µm, and 25 µm, respectively. FIB cross-section images of the 1-layer and 3-layer ink are shown in Figure 1(b) and (c), respectively. The average thickness of the TPU substrate is 127 µm.

### 2.2. Monotonic Experiments

The monotonic tension experiments were performed on a number of 1, 2, and 3-layered specimens with 2 mm and 0.5 mm trace widths to obtain the electrical resistance response to tensile strain. The monotonic tension experiments were performed using the Linkam Scientific TST350 Microtensile Test Stage at a strain rate of 2% per second, while the electrical resistance is measured using the Agilent 34401A digital multimeter (see Figure 1(d)). The resistance is reported as the normalized value  $R/R_0$ , where R is the resistance at strain  $\varepsilon$  and  $R_0$  is the initial resistance before deformation. Due to the distance  $d_{clamp}$  between the specimen clamps (about 30 mm) being shorter than half the overall length  $l_{print}$  of the double trace line (38 mm), the initial resistance  $R_0$  needed to be adjusted for the unstrained of the specimen:

$$R_0 = R_{measured, \varepsilon = 0} \times \left(\frac{d_{clamp}}{l_{print}/2}\right)$$

The resistance R is the sum of the initial resistance  $R_0$  and the measured change in resistance  $\Delta R$ , which is entirely attributed to the strained portion of the specimen.

$$\Delta R = R_{measured.\varepsilon} - R_{measured.\varepsilon=0} \tag{2}$$

$$R = R_0 + \Delta R \tag{3}$$

The initial resistance  $R_0$  for for the 1-, 2-, and 3-layer inks with 0.5 and 2 mm width, are plotted in Figure 1(e).

#### 2.3. Fatigue Experiments

The fatigue (cyclic tensile stretching) experiments were performed using the same setup as the monotonic tension experiments. In a fatigue experiment, a cyclic loading scheme was implemented with a mean strain of  $\varepsilon_m$  and strain amplitude of  $\varepsilon_a$ . The specimen was first elongated to a maximum strain of  $\varepsilon_m$ +  $\varepsilon_a$ , then strain cycled between the minimum strain  $\varepsilon_m$ -  $\varepsilon_a$  and maximum strain  $\varepsilon_m$ +  $\varepsilon_a$ . A strain rate of 2% per second was also used for the fatigue experiments.

The ink electrical resistance R cycles between a maximum and minimum during every loading cycle, and the maximum R during a stretching cycle increases with cycling. The rate of change in  $R/R_0$  with respect to cycles, or  $(R/R_0)'$ , at cycle N was calculated by fitting a linear regression function to the  $R/R_0$  maxima for a set of cycles between N-4 and N+4, excluding any null points at the beginning or end of the set of cycles. The choice of using the cycles N-4 to N+4 for the linear regression fitting was made by trial to achieve the generally smooth evolution of  $(R/R_0)'$  over the cycles.

### 2.4. In situ Experiments

In-situ monotonic tension and fatigue experiments were also performed under an Olympus LEXT 4100 confocal microscope. The monotonic experiments were paused at intervals of strain and the fatigue experiments were paused at intervals of cycles in order to capture *in-situ* optical images and laser profilometry scans of the ink surface at the maximum strain during the cycle. The optical images provided measurements of the length and density of the cracks on the ink surface. The laser profilometry scans characterized the ink surface topography and therefore the crack width. Both the optical images and laser profilometry scans were taken at a resolution of 0.62 μm/pixel and had approximate dimensions of 639 × 639 μm. *In-situ* monotonic tension experiments were performed with 3-layer 2 mm, 1-layer 2 mm, 3-layer 0.5 mm, and 1-layer 0.5 mm specimens to examine the effect of ink thickness and trace width on the crack pattern in the ink under tensile strain. *In-situ* fatigue experiments were performed with 3-layer 2 mm, 1-layer 2 mm, and 3-layer 0.5 mm specimens to examine the effect of cyclic loading on crack width.

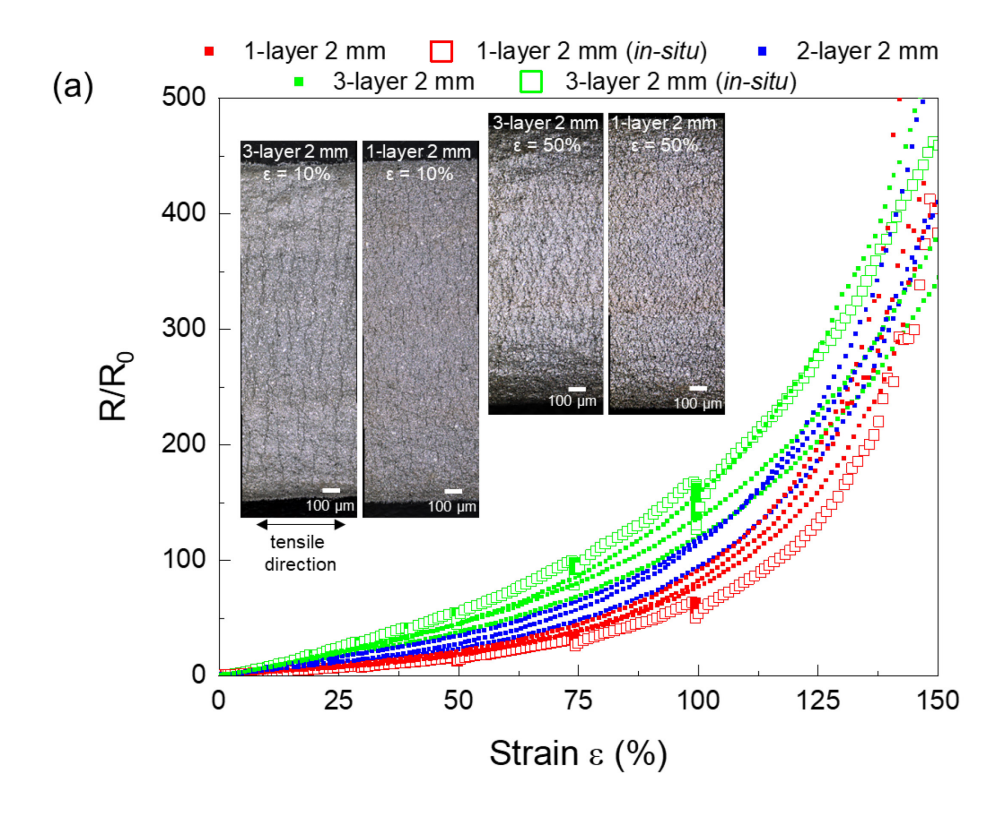
A separate *in-situ* experiment was performed inside the Thermo Helios 5 CX focused ion beam-scanning electron microscope (FIB-SEM). The experiment consisted of a monotonic tension experiment on a 3-layer 1 mm specimen paused at intervals of strain to capture *in-situ* SEM images of the ink surface, followed directly by a fatigue (cyclic tensile stretching) experiment on the same specimen paused at intervals of cycles to capture *in-situ* SEM images of the ink surface. The *in-situ* SEM experiment was performed on a Kammrath & Weiss MZ0-1 tension/compression testing module (narrow version). The distance between the grips was 15 mm and both the monotonic and fatigue experiments were performed at a strain rate of 0.133% per second. The digital image correlation (DIC) used to analyze the SEM *in-situ* images was performed using the Ncorr software

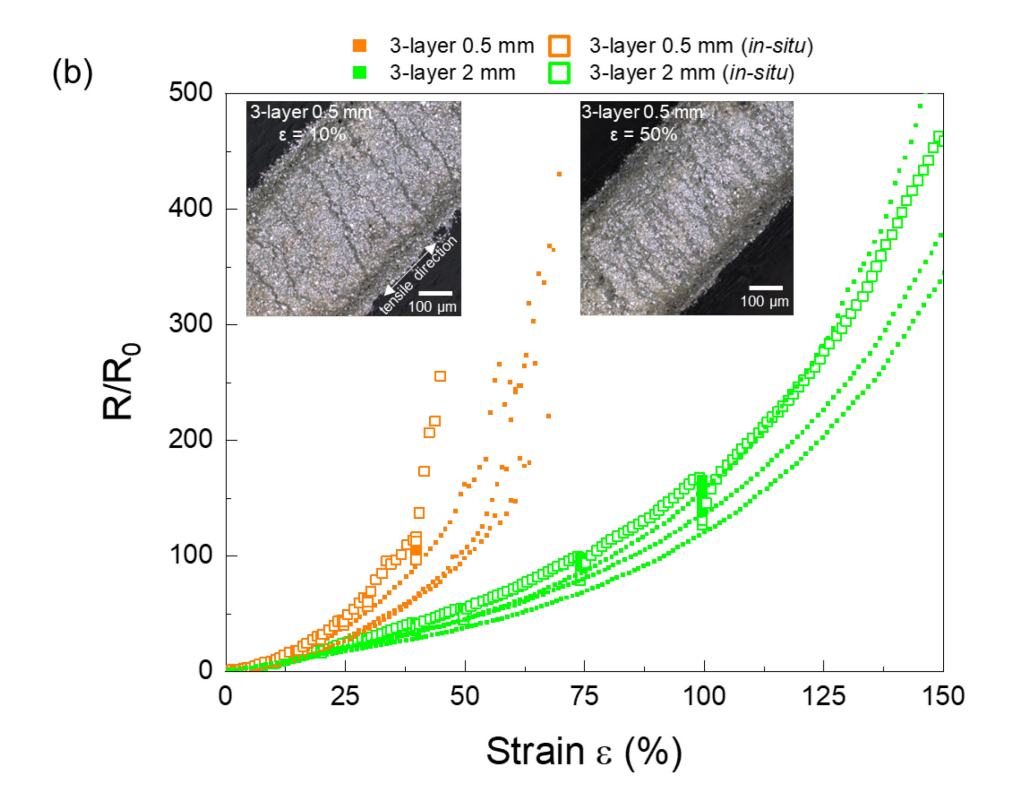
<sup>49</sup>. In addition, an *ex-situ* fatigue experiment was performed using the Linkam testing stage at a strain rate of 0.2% per second to obtain the expected R/R<sub>0</sub> evolution data.

#### 3. RESULTS AND DISCUSSION

#### 3.1. Monotonic Behavior

Figure 2(a) shows the effect of number of layers on the normalized resistance ( $R/R_0$ ) – applied strain ( $\epsilon$ ) data for the monotonic tensile stretching experiments (up to 150% strain) with 2-mm-wide specimens, while Figure 2(b) shows the effect of specimen width for the 3-layer specimens. The initial  $R_0$  values for the different specimen configurations are also plotted in Figure 1(e). Figure 2(a) shows that, for a given strain, the normalized resistance increases with number of layers. However, when accounting for the thickness effect on  $R_0$  (Figure 1(e)), the results show that, at a given strain, the resistance slightly decreases with increasing number of layers. This is clearly shown in Figure 2(c) where the ratio of normalized resistance,  $R/R_0$ , is plotted, for both 2 vs 1 layer and 3 vs 1 layer. Comparing 3 layers vs 1 layer, the ratio of normalized resistance is always less than 2.5, while the ratio of initial resistance (1 layer vs 3 layers) is 2.55 (as expected based on the measured thicknesses of 10  $\mu$ m for 1 layer and 25  $\mu$ m for 3 layers; see Figures 1(b) and (c)). Hence these results demonstrate that using thicker inks decreases the overall resistance even at large strains.





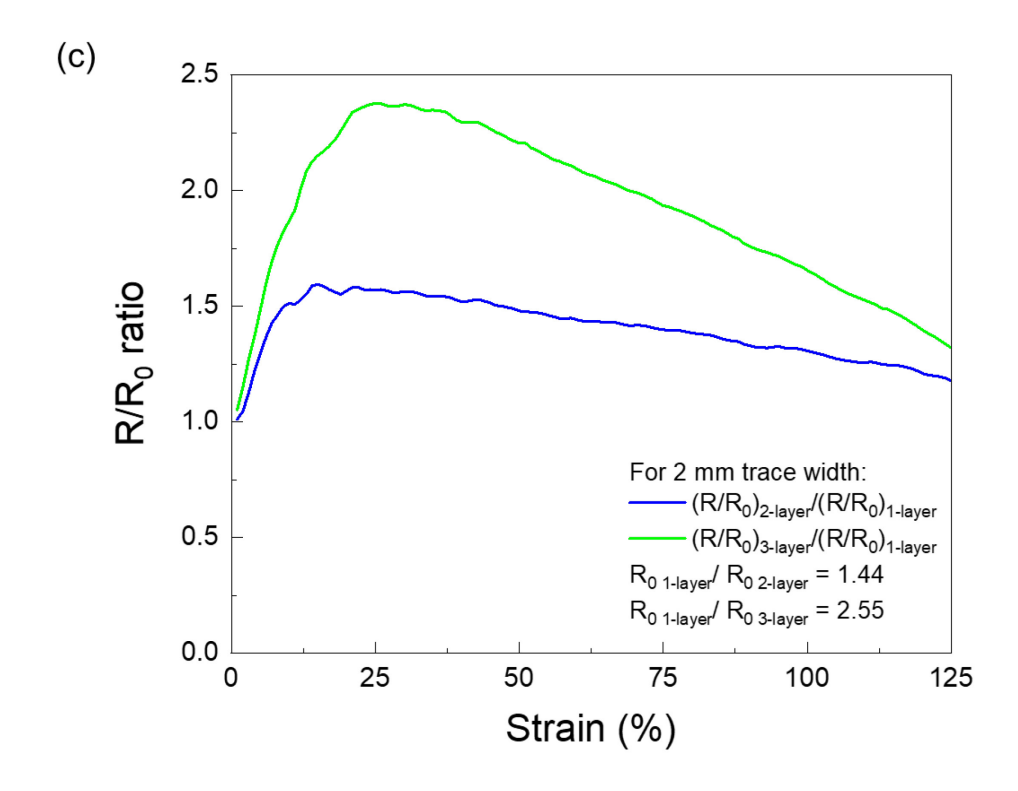


**Figure 2**.  $R/R_0$  =  $\epsilon$  evolution from monotonic stretching tests and crack pattern images from *in-situ* confocal microscope monotonic stretching tests for (a) 2 mm specimens with 1, 2, and 3 ink layers and (b) 3-layer specimens with 0.5 mm and 2 mm trace widths; (c)  $R_0$  for specimens of different layers and trace widths in monotonic tests.

Figure 2(b) shows that the  $R/R_0$  of the 3-layer 0.5-mm-wide specimens increased much more quickly with  $\epsilon$  than the 2-mm-wide specimens. Therefore, the trace width effect found by Cahn et al. <sup>48</sup> in the 1-layer ink can be extended to multi-layer inks. In other words, the width should be 2 mm or more to minimize both normalized resistance and resistance (since wider traces have lower  $R_0$ ) with strain.

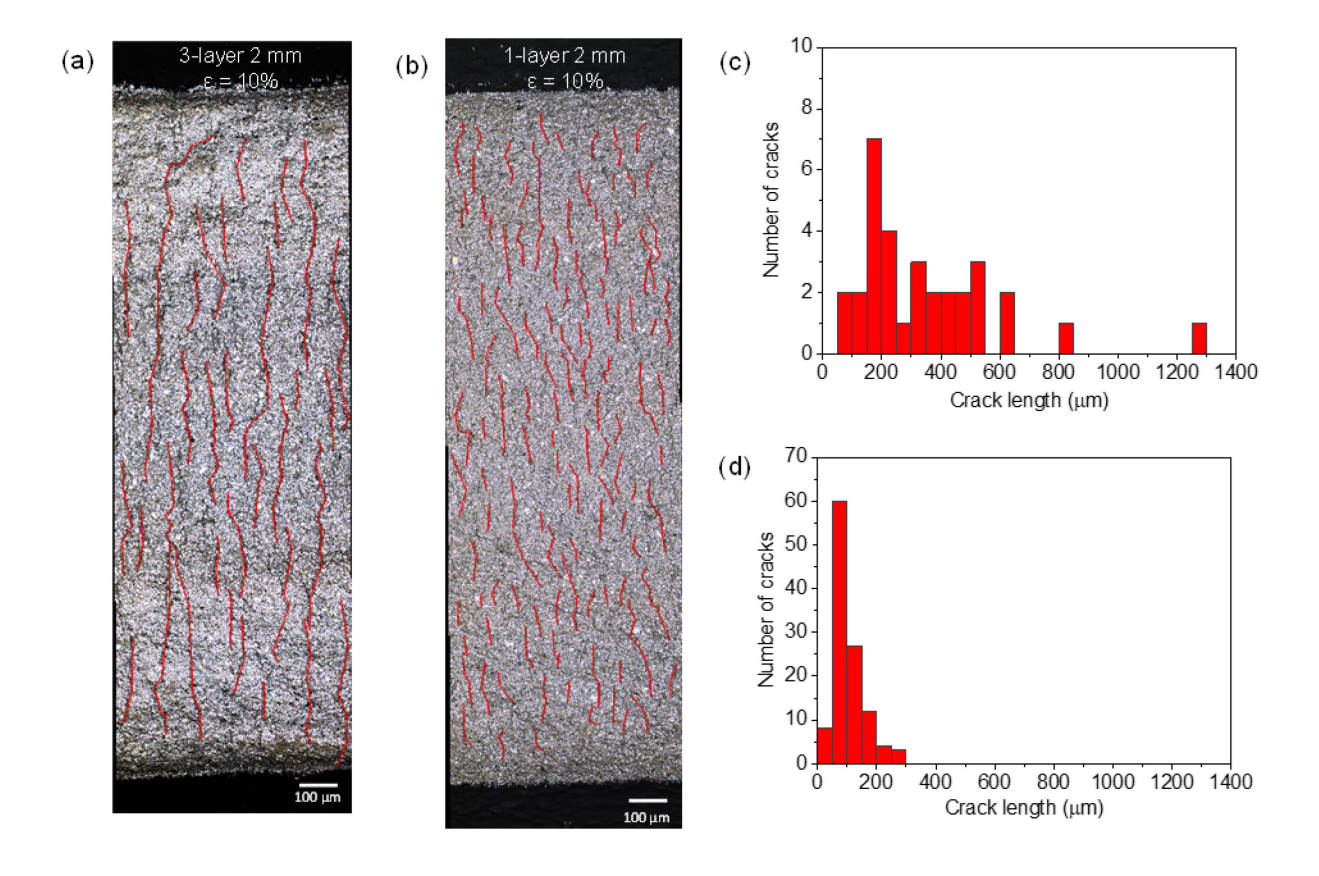
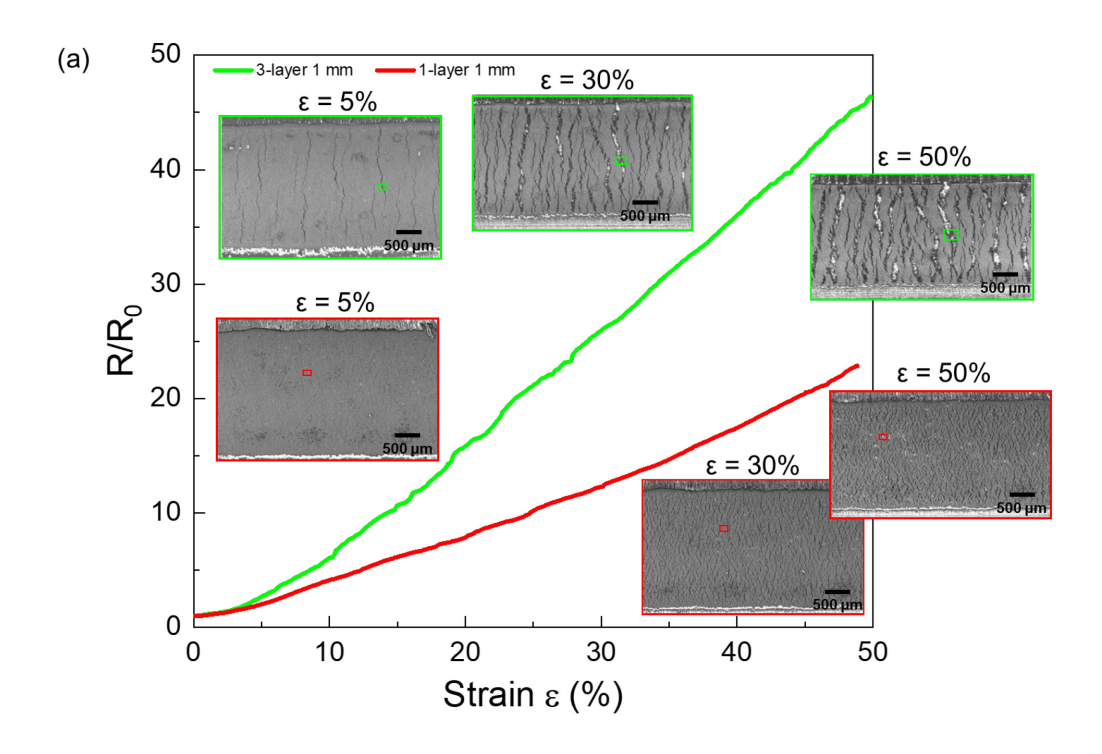
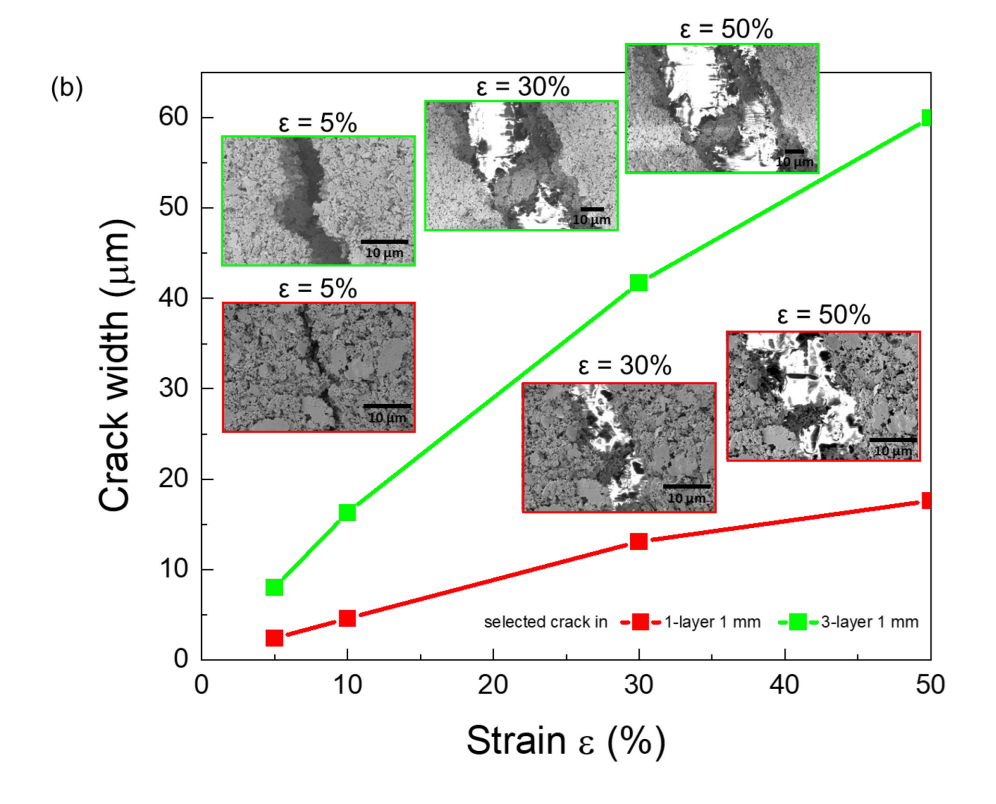


Figure 3. Crack patterns at  $\varepsilon = 10\%$  with cracks highlighted for (a) 3-layer 2 and (b) 1-layer 2 mm specimens; distribution of crack lengths for shown crack patterns of (c) 3-layer and (d) 1-layer 2 mm specimens.

The ink thickness and trace width effects can be understood by the observation of the crack pattern in the *in-situ* monotonic stretching experiments. From the confocal optical images for the 1-layer and 3-layer 2-mm-wide specimens (Figure 2(a)), the lengths and area density of the cracks in the specimens with different ink thicknesses could be analyzed. The surface cracks in these two specimens at 10% strain, identified by visual inspection, are highlighted in Figure 3(a) and (b). The lengths of the cracks are sorted in the histograms of Figure 3(c)-(d). The mean crack length was 347 µm for the 3-layer and 102 µm for the 1-layer 2 specimen. For the 3-layer specimen, a significant number of cracks had lengths exceeding 0.5 mm; for the 1-layer

specimen, none of the cracks exceeded a length of 0.3 mm. The area density of the cracks in a specimen was calculated by dividing the total crack count by the observed area. The area crack density was about 27 cracks per mm² for the 3-layer and 95 cracks per mm² for the 1-layer specimen at 10% strain. Therefore, the 1-layer specimen had a network of more numerous, shorter cracks while the 3-layer specimen had a network of fewer, longer cracks. The greater lengths of the cracks in the 3-layer specimen, some of which exceeded 0.5 mm (Figure 3), enabled the traversal of the entire 0.5 mm trace width by some of the cracks in the 3-layer 0.5-mm-wide specimen (Figure 2(b)). At higher strains (>50%), the cracks in the 3-layer ink traversing the 0.5 mm trace line were observed to widen drastically, leading to a rapid increase in  $R/R_0$ . In the cases where the cracks were not able to traverse the entire trace width, such as the 2-mm and 1-mm-wide specimens or the 1-layer 0.5-mm-wide specimen (see Figure S1 in the Supporting Information), the cracks were observed to coalesce at some junctions and also branch into subcracks as  $\epsilon$  increased (Figure 2(a) and 3). The increase in  $R/R_0$  with strain was not as significant in these cases.





**Figure 4.** (a) Crack pattern images from *in-situ* SEM monotonic stretching tests with  $R/R_0$ – $\varepsilon$  evolution from corresponding *ex-situ* tests; (b) close-up images of representative cracks from *in-situ* SEM monotonic stretching tests with crack width– $\varepsilon$  evolution.

Figure 4 shows SEM images of the crack pattern from the monotonic part of the *in-situ* SEM experiments with the 3-layer and 1-layer 1-mm-wide specimens and the  $R/R_0 - \varepsilon$  data from the corresponding *ex-situ* experiments. Similar to the optical images for the 2-mm-wide specimens in Figure 1, the low magnification SEM images in Figure 4(a) also showed a clear distinction between the longer cracks in the 3-layer ink and the shorter cracks in the 1-layer ink. At 30% strain, crack coalescence traversing more than 50% of the trace line had already occurred at several locations within the imaged area for the 3-layer specimen, while the shorter and more numerous cracks in the 1-layer specimen could not coalesce into such long cracks even at 50% strain. Besides being longer, Figure 4(a) also showed that the cracks in the 3-layer ink were also notably wider. Figure 4(b) shows higher magnification images of the crack width  $-\varepsilon$  evolution for selected cracks in the 3-layer and 1-layer specimens. The two selected cracks were representative of the widest, most well-developed cracks in the respective specimens. Both cracks were observed to widen and deepen simultaneously. The width of the crack in the 3-layer specimen was consistently 3 to 4 times the width of the crack in the 1-layer specimen up to an  $\varepsilon$  of 50%. Hence it is clear that crack widening, as well as deepening, is influenced by the ink thickness. For  $\varepsilon = 30\%$ , both of the selected cracks in Figure 4(b) had clearly deepened to the ink-substrate interface and widened to more than 10 µm apart, with no contact between the silver flakes (whose sizes range from hundreds of nm to several µm) on the two crack faces. However, in both the 3-layer and 1-layer specimens, there

were also some cracks and sections of cracks that did not appear to be wide enough to be throughthickness even at  $\varepsilon = 50\%$ .

Based on the above results, it can be seen that the different  $R/R_0 - \varepsilon$  evolution behaviors for varying ink thickness correlates strongly with the corresponding differences in the crack pattern. The impact of ink thickness on the crack pattern at a given  $\varepsilon$  can be understood by the following fracture mechanics relation between the energy release rate  $\mathcal{G}$  of a crack in a thin film and the film thickness  $h^{50-51}$ .

$$G = \left(\frac{\sigma_0^2 h}{\bar{E}_f}\right) Z \tag{4}$$

The energy release rate  $\mathcal{G}$  is proportional to the film thickness h. The proportionality is determined by the stress  $\sigma_0$  on the crack faces, the plane strain elastic modulus  $\overline{E}_f = E_f/(1-v_f^2)$  of the film where  $E_f$  and  $v_f$  are respectively the ink elastic modulus and Poisson's ratio, and the dimensionless number Z depending on the Dundur's parameters  $\alpha$  and  $\beta$  as well as dimension ratios including the ratio H/h between the substrate thickness H and ink layer thickness h. Hence the driving force for crack extension in the 3-layer ink is expected to be roughly 3 times that of the 1-layer ink. In addition, the dependence of Z on H/h means that  $\mathcal{G}$  is greater for a larger h given the same H, especially for  $H/h > 10^{52}$ . For the 1-layer and 3-layer ink specimens, the H/h ratio is about 5 and 13 respectively. This difference is expected to increase the  $\mathcal{G}$  of the 3-layer ink to slightly more than 3 times that of the 1-layer ink.

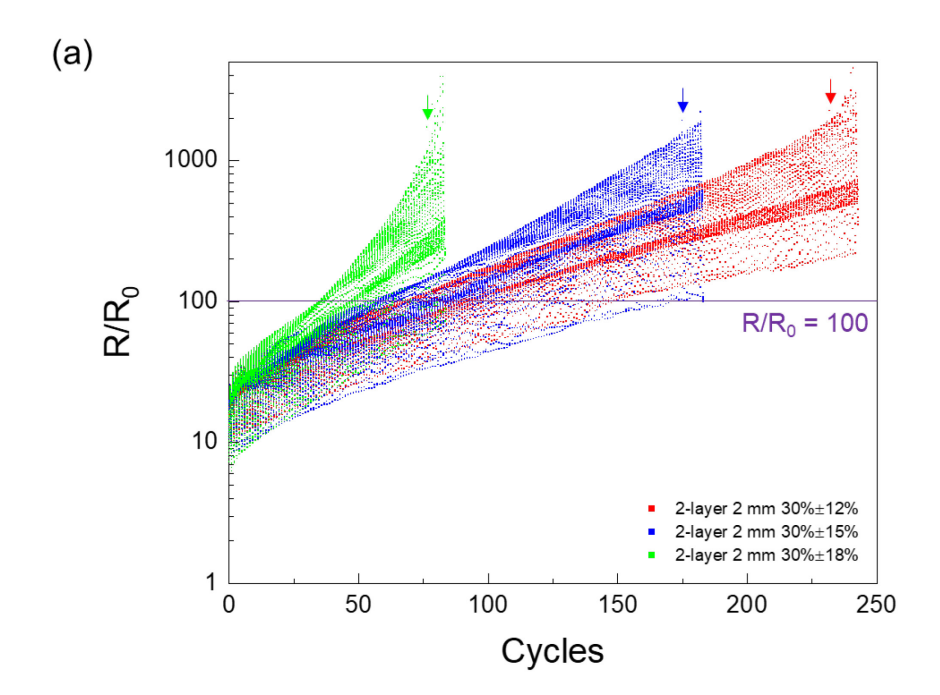
The greater driving force for crack extension for the 3-layer ink corroborates with the observed longer cracks in the 3-layer ink compared to the 1-layer ink. The effect of the crack pattern on electrical resistance was investigated by Glushko et al. <sup>53</sup> for metallic films on polymer

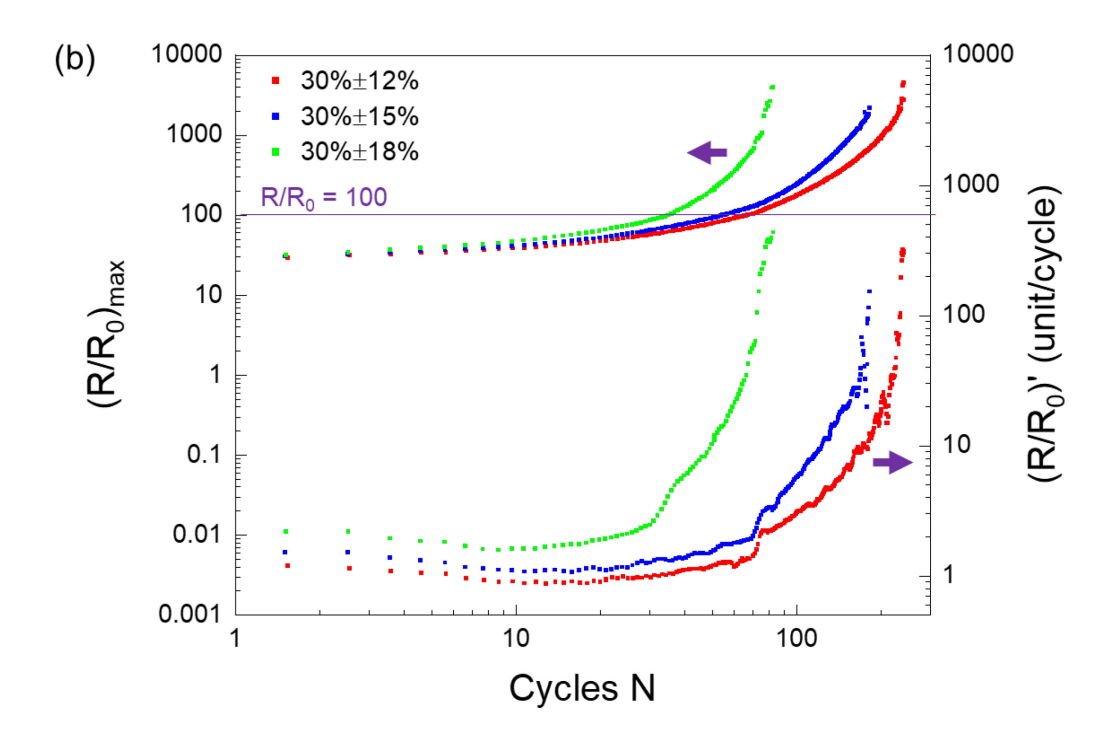
substrates. From finite element modeling results, the normalized resistance was found to increase with the fourth order of crack length and second order of area crack density. Using their relationship and the average crack length and area crack density found in Figure 3, the  $R/R_0$  was calculated to be 2.2 for the 1-layer and 8.5 for the 3-layer 2 mm specimen at an ε of 10%. The corresponding average R/R<sub>0</sub> from the experiments were 3.68±0.35 and 6.88±0.47, respectively. The predicted  $R/R_0$  are not too far off, highlighting the significant effect of the crack pattern, especially the crack length, on resistance evolution. However, the model by Glushko et al. assumes through-thickness cracks that are perfectly insulating, a reasonable assumption for metallic (i.e., stiff) thin films on compliant polymer substrates. In the case of the PE874 conductive ink, not all cracks are through-thickness, especially at lower applied strains, as was shown in Figure 4. Given that the same silver flakes (with sizes ranging from several µm to hundreds of nm) were used in the 1-layer and 3-layer ink, the greater width of the cracks in the 3-layer ink meant that a smaller portion of the total crack face area would be bridged by the silver flakes compared to the 1-layer ink at the same level of  $\varepsilon$ . Therefore the widening and deepening of the cracks could be a secondary mechanism causing the difference in  $R/R_0 - \varepsilon$  evolution with varying ink thickness, other than the crack length dependence on ink thickness.

## 3.2. Cyclic Behavior

Uniaxial cyclic stretching (fatigue) experiments were used to study the effect of repeated deformation on the conductive ink. Figure 5(a) shows the  $R/R_0$  evolution with cyclic tensile stretching for three fatigue tests with a mean strain  $\epsilon_m$  of 30% and different strain amplitudes  $\epsilon_a$  of 12%, 15%, and 18%. The electrical resistance of the ink cycles between a maximum and minimum during every loading cycle. The maximum  $R/R_0$  during the loading cycle steadily increases as the number of cycles increase, but eventually a point of instability is reached where  $R/R_0$  no longer

increases steadily but experiences irregular jumps of increase with further cycling. In Figure 5(a), the onset of instability is marked by the colored arrows. For these three tests, the onset of instability occurred at a high  $R/R_0$  of 800 or above. Figure S2 in the Supporting Information shows the  $R/R_0$  at the onset of instability plotted against the number of cycles to instability  $N_{instability}$  for all fatigue tests excluding the *in-situ* ones. For most of the tests, the onset of instability occurred at a  $R/R_0$  higher than 100. Therefore, we define the fatigue life  $N_f$  by the number of cycles until a  $R/R_0$  of 100 is reached. In the previous work by Cahn et al. <sup>47</sup>, fatigue life was instead defined by the number of cycles until a  $R/R_0$  of 500 is reached.

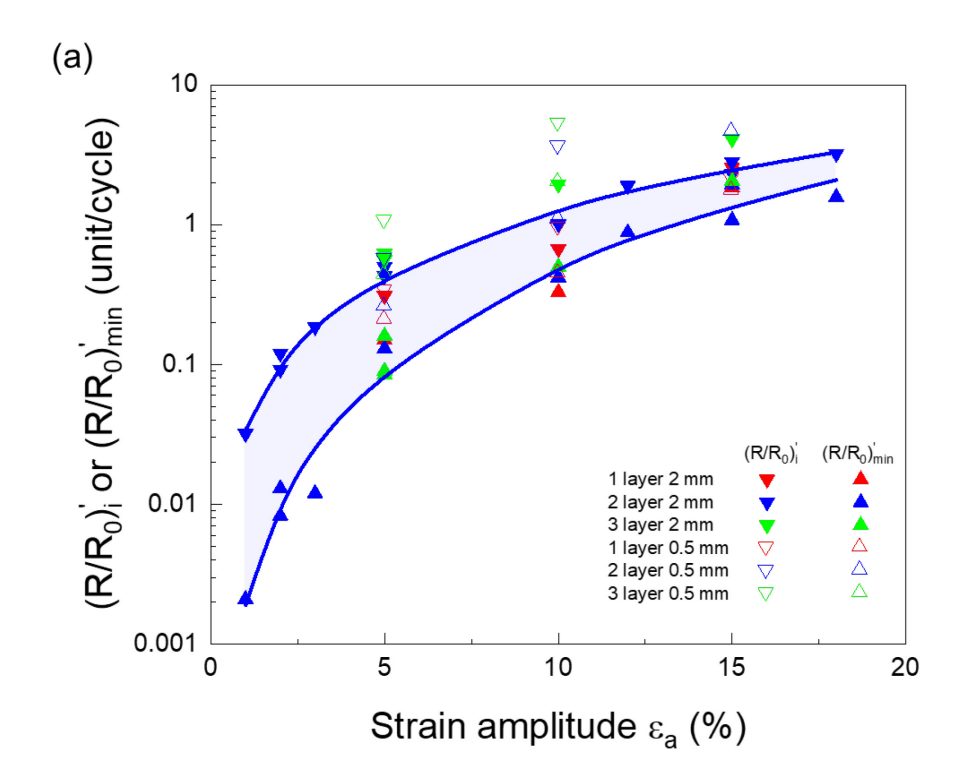




**Figure 5.** (a) R/R<sub>0</sub> evolution over cycles for the 2-layer 2 mm tests at strains 30% $\pm$ 12%, 30% $\pm$ 15%, and 30% $\pm$ 18%; (b) R/R<sub>0</sub> maxima over cycles and rate of change in normalized resistance with cycles (R/R<sub>0</sub>)' for forementioned tests.

Figure 5(b) shows the  $R/R_0$  maxima per cycle for the three forementioned tests as well as the rate of change in  $R/R_0$  with respect to cycles  $N-d(R/R_0)/dN$  or  $(R/R_0)'$  for shorthand. A value of  $(R/R_0)'=1$  means that  $R/R_0$  increases by 1 every cycle. The rate  $(R/R_0)'$  is found to always decrease during the initial portion of the fatigue test, and is therefore at a local maximum on cycle 1. For the tests with a large strain amplitude  $(\epsilon_a > 10\%)$ , as illustrated in Figure 5(b),  $(R/R_0)'$  decreases to a minimum within the first 20 to 30 cycles, and then increases steadily until the onset of instability. The normalized resistance  $R/R_0$  has not reached 100 when the rate reaches its minimum. However, once the rates have significantly increased (i.e.,  $(R/R_0)' > 5$  or 10),  $R/R_0$  has well exceeded 100: for practical purposes, the ink is not functional anymore at that stage. For tests

with a small strain amplitude ( $\epsilon_a \le 5\%$ ), (R/R<sub>0</sub>)' does not see any increase with cycling, but instead sees a phase of slower decrease or plateauing until the onset of instability (see Figure S3 in the Supporting Information showing an example of the (R/R<sub>0</sub>)' evolution for  $\epsilon_a = 1\%$ ). Hence, the initial rate of resistance increase, (R/R<sub>0</sub>)'<sub>i</sub>, is a relevant parameter, which for example could be used to predict resistance evolution in a conservative manner, given that it is a local maximum.



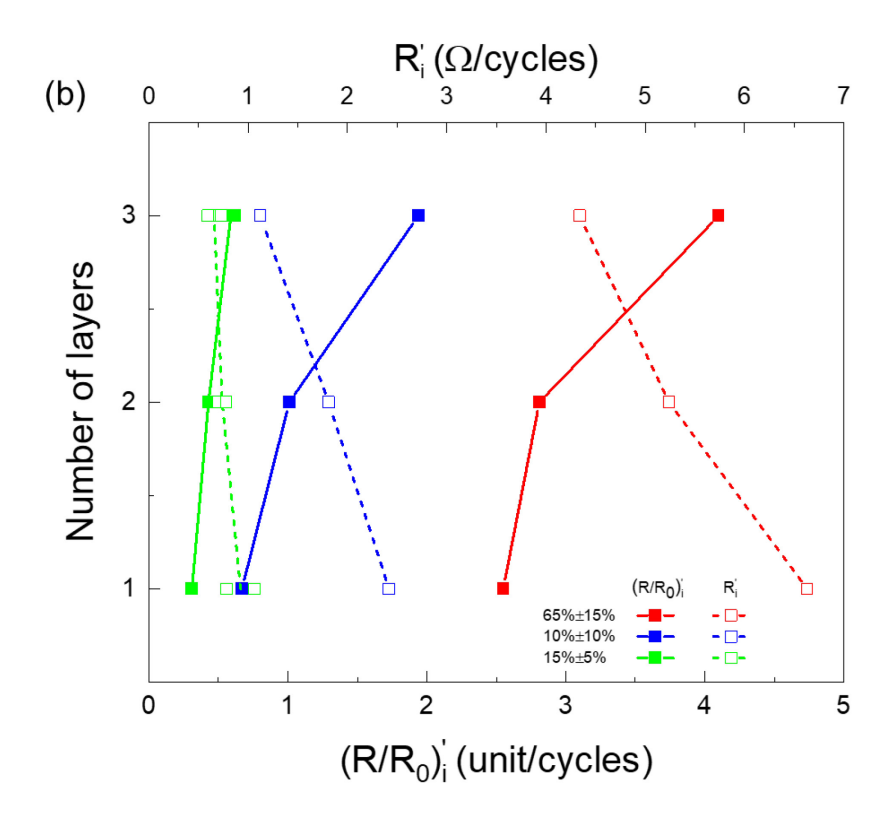


**Figure 6.** (a)  $(R/R_0)'_i$  and  $(R/R_0)'_{min}$  versus strain amplitude; (b) number of ink layers versus  $(R/R_0)'_i$  and  $R'_i$ 

Figure 6(a) shows the initial (local maximum) and the minimum  $(R/R_0)'$  for all tests in the current work, plotted against the strain amplitude  $\epsilon_a$ . Both  $(R/R_0)'_i$  and  $(R/R_0)'_{min}$  showed a strong correlation with  $\epsilon_a$ , as highlighted by the blue trend lines in Figure 6(a). Results from the tests with the 2-layer 2-mm-wide specimens show that between strain amplitudes of 1% and 19%,  $(R/R_0)'_i$  increased by about 2 orders of magnitude from 0.032 to 3.22. The difference between  $(R/R_0)'_i$  and  $(R/R_0)'_{min}$  as indicated by the blue envelope was much greater at the  $\epsilon_a$  of 1% (more than an order of magnitude) than at the  $\epsilon_a$  of 18% (about only 2 to 3 times). The effect of the mean strain  $\epsilon_m$  on  $(R/R_0)'$  appears to be much less significant, based on the two specimens tested at  $\epsilon_a$  = 2% having similar rates despite having different  $\epsilon_m$  (15 vs 60%). Trace width appears to have a significant

effect on  $(R/R_0)'$ , with the 0.5-mm-wide specimens generally having a higher  $(R/R_0)'_i$  and  $(R/R_0)'_{min}$  than the 2-mm-wide specimens.

Figure 6(b) shows  $(R/R_0)'_i$  plotted against the number of ink layers for the 65%±15%,  $10\%\pm10\%$ , and  $15\%\pm5\%$  tests. The  $(R/R_0)'_i$  increased with ink thickness, especially for the 65%±15% and  $10\%\pm10\%$  cases. For practical purposes, however, the rate of change in resistance R with cycles dR/dN (or R'for shorthand) is the more useful parameter than  $(R/R_0)'$  in characterizing resistance increase across different ink geometric dimensions. Figure 6(b) also shows that  $R'_i$  decreased with ink thickness, which corresponds to a slower increase in R with cycling and a longer fatigue life. Therefore, thicker ink layers are beneficial to keep the resistance low after repeated deformation.

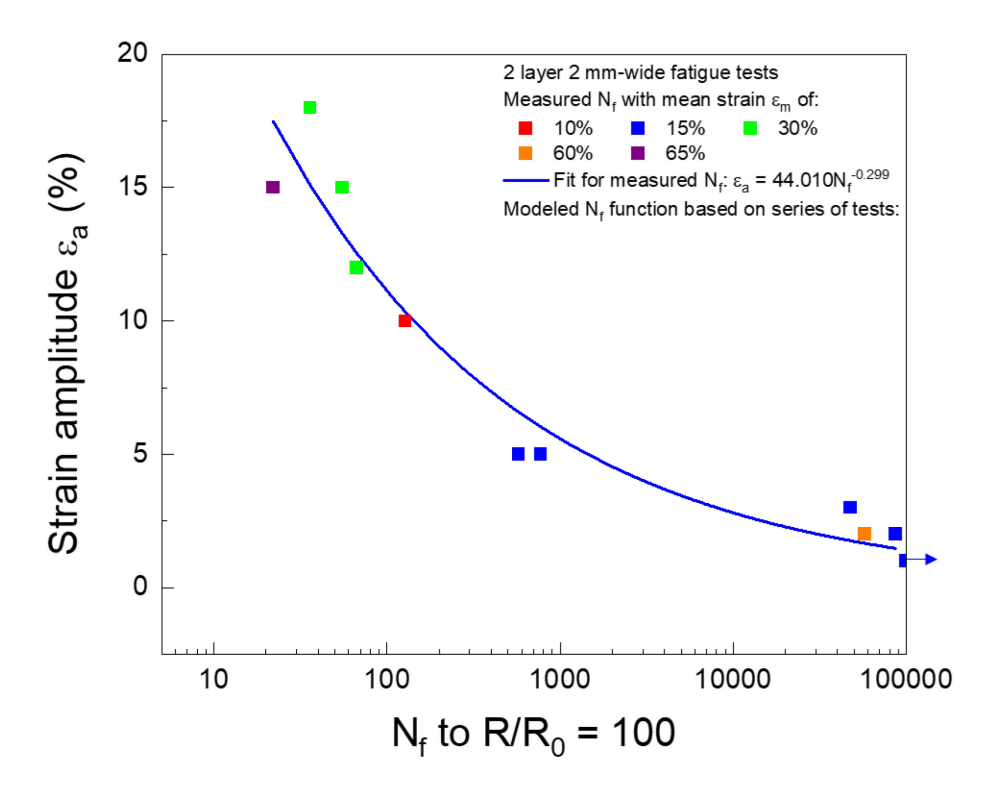


**Figure 7.** Strain amplitude versus measured \ fatigue life N<sub>f</sub>;

Figure 7 shows the strain amplitude  $\epsilon_a$  - fatigue life  $N_f$  curve, for all tests with 2-layer 2-mm-wide specimens. The measured  $N_f$  ranges from 36 cycles for the 30%±18% test to over 100,000 cycles (run-out test) for the 15%±1% test. There exists a strong correlation between measured  $N_f$  and  $\epsilon_a$ , which was fitted to a power law function in that figure. Other than  $\epsilon_a$ , the mean strain  $\epsilon_m$  also affects  $N_f$ . For example,  $N_f$  was 86,533 cycles for the 15%±2% test, but only 57,572 cycles for the 60%±2% test. The  $\epsilon_m$  effect on  $N_f$  is likely mainly due to its effect on  $R/R_0$  at the maximum applied strain (equaling  $\epsilon_m + \epsilon_a$ ) during the first cycle. However,  $\epsilon_a$  has a more significant effect on  $N_f$  than  $\epsilon_m$ . The relative importance of  $\epsilon_a$  and  $\epsilon_m$  in determining  $N_f$  is highlighted by comparing the 60%±2% test ( $N_f$  = 57,572 cycles) with the 15%±5% tests ( $N_f$  < 800 cycles).

To better understand the ink deformation mechanisms responsible for the resistance increase with cyclic stretching, *in-situ* confocal microscope and SEM fatigue experiments were performed for this work.

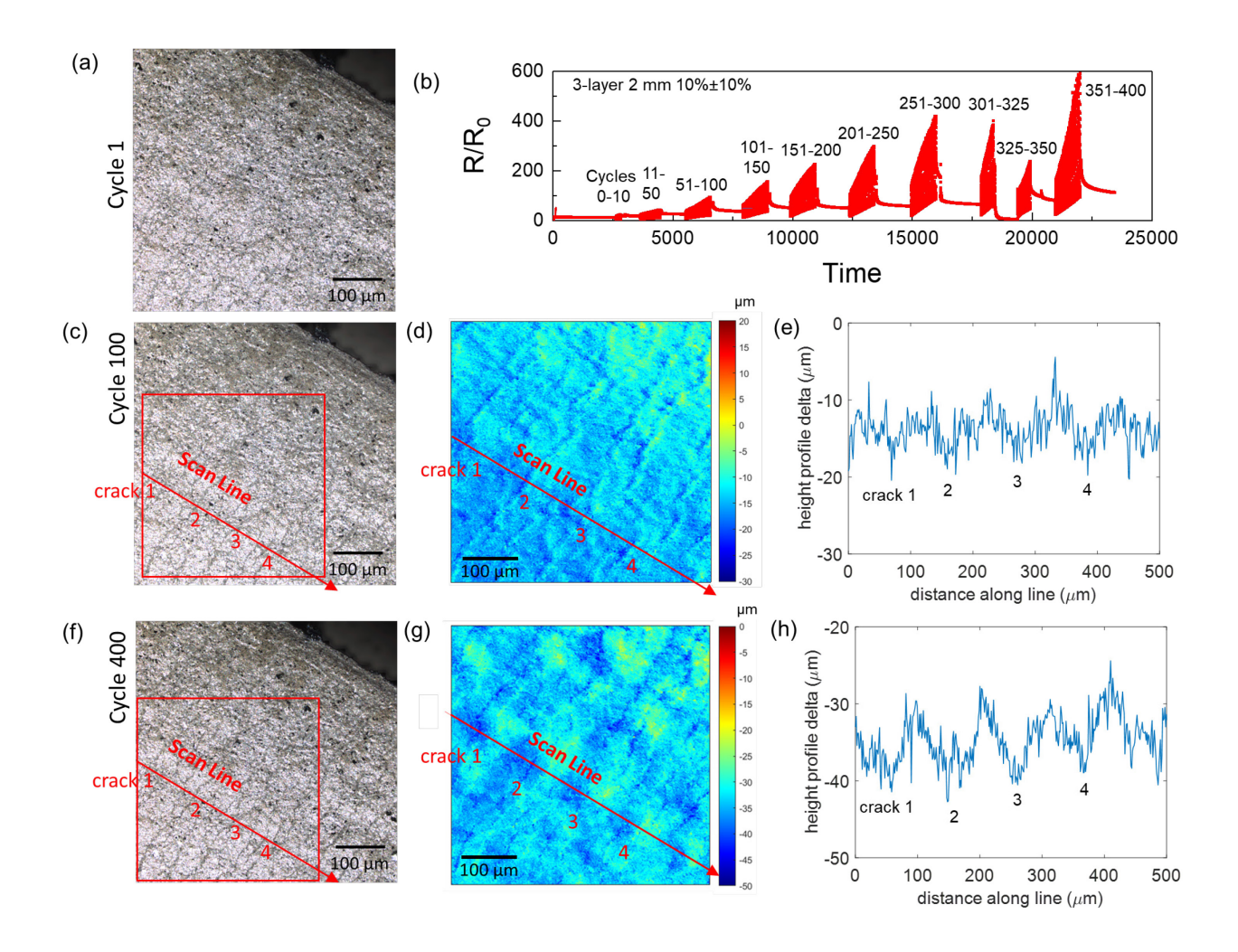


**Figure 8.** (a) Optical image at maximum strain on cycle 1 from *in-situ* confocal microscope cyclic stretching test; (b)  $R/R_0$  evolution over cycles; (c) optical image at maximum strain on cycle 100; height profile delta map (d) and height profile delta line scan (e) between cycles 1 and 100; (f) optical image at maximum strain on cycle 400; height profile delta map (g) and height profile delta line scan (h) between cycles 1 and 400.

The *in-situ* confocal microscopy fatigue experiment was performed at lower strains than in <sup>47</sup> to examine the evolution of the ink surface topography, particularly the surface cracks, over the cycles. A 3-layer 2-mm-wide specimen was cycled at 10%±10% strain for 400 cycles under the optical and laser confocal microscope. Figure 8(a), (c), and (f) show the optical images at the

maximum strain during cycle 1, 100, and 400; Figure 8(b) shows the  $R/R_0$  evolution over the cycles. The fatigue life  $N_f$  was reached at 118 cycles, which is very close to the  $N_f$  of 121 measured in the *ex-situ* test. This *in-situ* confocal microscope experiment differed from the 65% $\pm$ 15% strain experiment with the 1-layer 0.5-mm-wide specimen performed by Cahn et al. <sup>47</sup> in that the 3-layer 2-mm-wide specimen was cycled at much lower strains, which should facilitate the examination of crack deepening with cycling since many of the cracks should not be through-thickness on cycle 1.

Superposing the laser profilometry scans of the same area taken during cycles 1 and 100 (or 400) at maximum strain, a height delta map between cycles 1 and 100 (or 400) can be generated by subtracting the ink height profile data for the two cycles pixel by pixel. The exact alignment of the laser profilometry data from the two cycles is performed with the aid of digital image correlation (DIC) in order to remove the small shifts in displacement between the two scans. A detailed explanation for the alignment process can be found in Cahn et al. <sup>47</sup>. Figure 8(d) and (g) show the height delta maps between cycles 1 and 150 and between cycles 1 and 400, respectively. Figure 8(e) and (h) show line scans over the height delta maps for cycles 1-100 and for cycles 1-400 along the red lines marked in Figures 8(d) and (e). For both the cycles 1-100 and cycles 1-400 height delta maps, a significant portion of the crack pattern had deepened with respect to their surrounding regions after cycling, though the in-plane crack pattern has remained the same. Based on the differences in the height delta data between cracks 1 to 4 and their surrounding regions in the line scans, the crack deepening occurred by an average of 10 µm between cycles 1 and 100 and 13 μm between cycles 1 and 400. Comparing the height delta maps and line scans for cycles 1-100 and cycles 1-400, some of the crack openings, most notably crack 3 and 4, also appeared to have widened while they deepened with cycling.

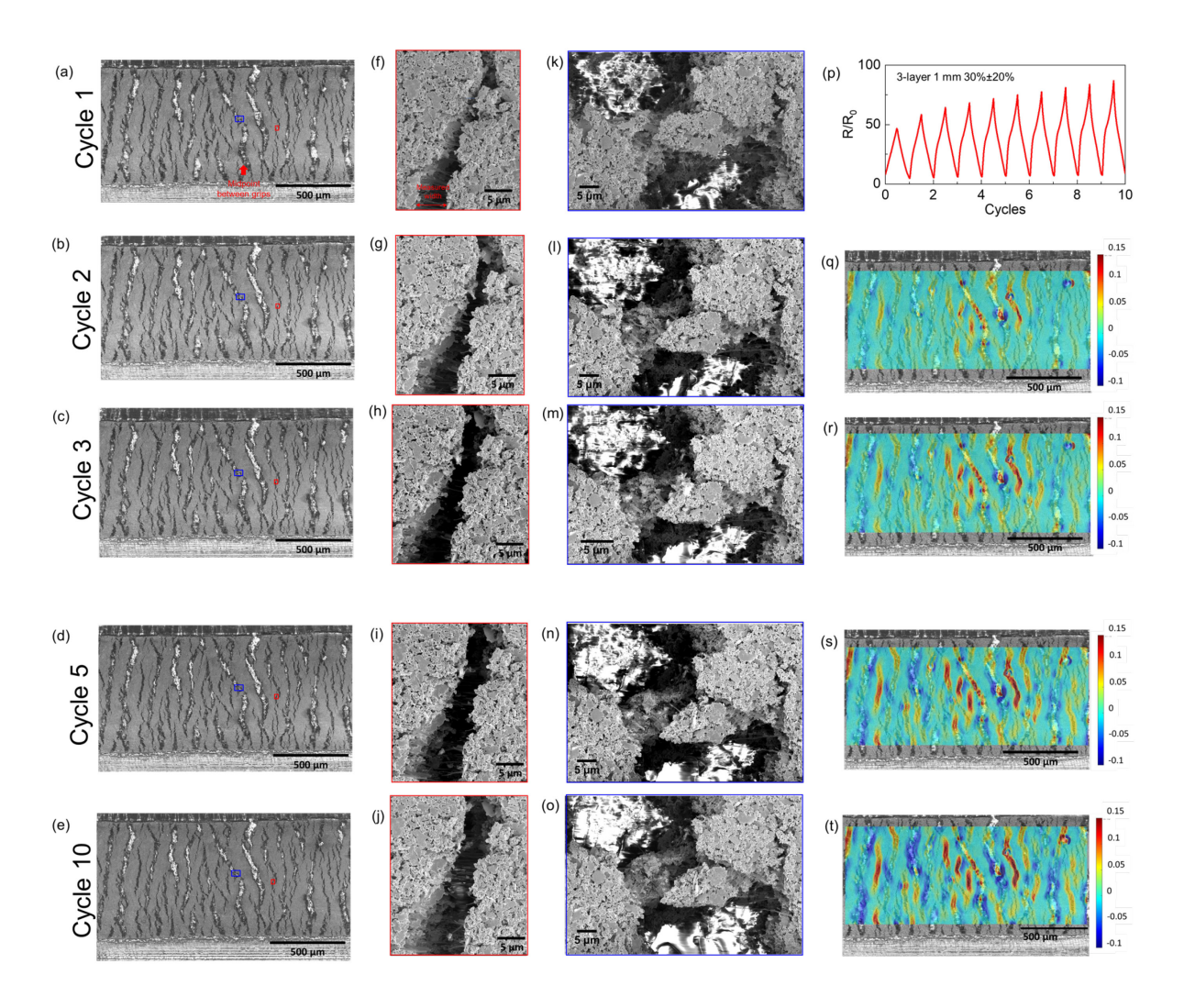


**Figure 9.** (a)-(e) Crack pattern images for cycles 1, 2, 3, 5, and 10 of *in-situ* SEM cyclic stretching test; closeup images of representative narrow crack (f)-(j) and wide crack with ink linkage (k)-(o) over the cycles; (p) R/R<sub>0</sub> evolution over cycles from corresponding *ex-situ* test; (q)-(t) DIC strain maps for cycles 2, 3, 5, and 10.

To obtain conclusive evidence of crack widening with cycling, a *in-situ* SEM experiment was performed to cyclically stretch a 3-layer 1-mm-wide specimen at strains of 30%±20%, after first monotonically stretching the specimen to an applied strain of 50% as a part of the first cycle

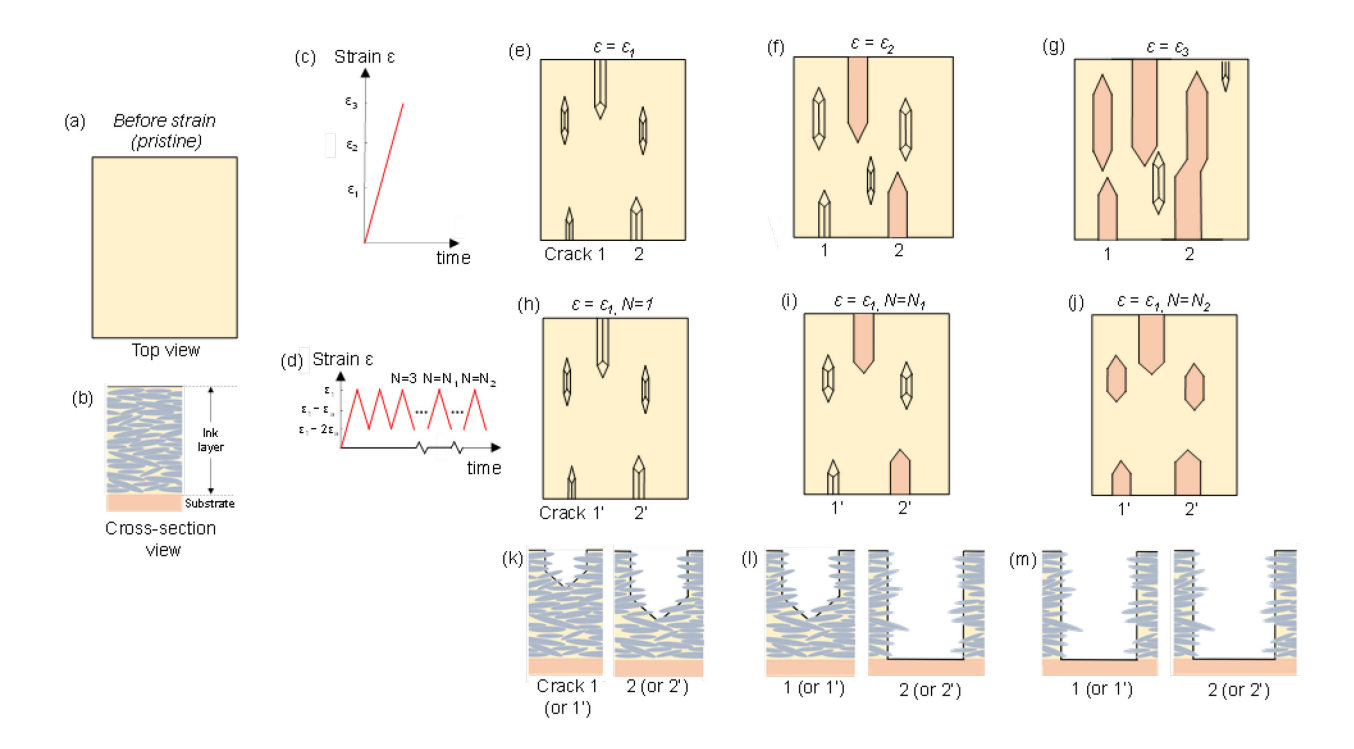
(Figure 3). Figure 9(p) shows the first 10 cycles of the  $R/R_0$  evolution from a separate *ex-situ* test; the SEM *in-situ* test was expected to have the same  $R/R_0$  evolution, with  $R/R_0$  reaching about 90 at cycle 10. Figure 9(a)-(e) show the crack pattern at 50% strain during cycles 1, 2, 3, 5, and 10 for a 1.75 mm long section of the trace line roughly centered at the midpoint between the grips of the testing stage. While the extent of the crack pattern appears to remain unchanged over the cycles at low magnification, higher magnification images of the cracks showed clear evidence of their widening with cycling.

Figure 9(f)-(j) show close-up images of the widening of a representative narrow crack over the cycles. On cycle 1, the width of the crack measured about 1.6 µm at the point marked in Figure 9(f). From cycle 1 to cycle 5, the width of the crack increased to about 6.4 μm. On cycle 1, the two cracks faces were very close to each other and the silver flakes could be seen to bridge the crack. By cycle 5, the crack faces were completely separated from each other and the silver flakes could no longer bridge the crack, likely resulting in a complete loss of electrical conductivity across that crack. Figure 9(k)-(o) show close-up images of the widening of a representative wide crack with an island of ink forming a linkage in the crack opening. From cycle 1 to cycle 2, the crack widened by about 3 µm on the left side. In the subsequent cycles, parts of the ink island were observed to shift and break off in a direction transverse to loading, causing damage the ink linkage across the crack opening. The damage evolution of the ink linkage observed in Figure 9(k)-(o) shows how fatigue damage could severe an otherwise conductive path across a wide crack opening. At higher applied strains (>30%), many of the apparently coalesced cracks were still separated at junctions by ink linkages that could provide conductive pathways. Fatigue damage to these ink linkages by crack widening likely represents a significant mechanism for reducing the electrical conductivity.

Figure 9(q)-(t) show the DIC tensile strain maps for the crack patterns at cycles 2, 3, 5, and 10 shown in Figures 9(b)-(e). The DIC strain maps used the image at 50% strain during cycle 1 (Figure 9(a)) as the reference image and the images at 50% strain during cycles 2, 3, 5, and 10 (Figure 9(b)-(e)) as the current images to obtain the tensile strain distribution generated from cycling. The crack widening, as shown by the positive strain distributions, were concentrated in the cracks near the midpoint between the grips on cycle 2. During the subsequent cycles, the cracks further away from the midpoint began to widen more, as can be seen in the progression of the strain maps for cycles 3 to 10. As some cracks widened, other cracks were compressed and narrowed, resulting in the negative strain distribution over them. In the area analyzed by the DIC strain maps, the ratio of the number of widening cracks to the number of narrowing cracks was about 2 to 1.

# 3.3. Degradation Mechanisms

The results of the *in-situ* SEM experiments, from both the monotonic and cyclic parts, showed that the basic mode of microstructure damage in the ink is the simultaneous widening and deepening of the cracks. One notable distinction in damage mechanism between monotonic strain increase and cycling between two strain values is that the crack length increased significantly during the former (i.e., with increasing applied strain) but remained unchanged during the latter (i.e., with increasing numbers of cycles). This key mechanistic difference is illustrated in Figure 10 by showing a series of schematic diagrams illustrating the damage mechanisms for the monotonic and cyclic scenarios, with the top and cross-section views for the ink layer mounted on the substrate.



**Figure 10.** Schematic diagrams showing the top view (a) and cross-section view (b) of the ink layer; the monotonic (c) and cyclic (d) straining scenarios; top view of the ink layer surface during monotonic (e)-(g) and cyclic (h)-(j) straining; cross-section view of the ink layer during monotonic and cyclic straining (k)-(m).

.

Knowing the difference in damage mechanism between the monotonic strain increase and cycling between two strain values, the electrical resistance increase during cyclic stretching to the same strain must therefore be entirely attributed to crack widening and deepening, whereas, as shown earlier, the lengthening of the cracks is a major contributor to resistance increase with increasing applied strain. The fact that the cracks do not lengthen with cycling means that the associated range in strain energy release rate,  $\Delta G$ , is not large enough to get fatigue-driven crack extension in the polyurethane binder of the ink. Instead, the widening of the cracks under cyclic loading is likely a result of unlocking of adjacent silver flakes during the repeated back-and forth

motion of the crack faces. Another possible fatigue mechanism for crack widening is the fatigue of the TPU substrate at the location of the cracks once they reach the interface, as suggested by a post-mortem (unloaded specimen) FIB cross section of a fatigued specimen (see red arrows in Figure S4 in the Supporting Information). This understanding of the fatigue damage mechanism in a conductive ink is in agreement with the observed relation between fatigue resistance increase and through-thickness cracking for a polymer-supported metal thin film found by Gebhart et al. <sup>54</sup>.

This work showed that ink thickness and trace width impact the electrical resistance evolution with tensile strain under monotonic and cyclic loading, due to differences in crack pattern resulting from stretching. For practical applications, thicker (≥25 µm) and wider (≥2 mm) inks should be used to lower R increases with repeated deformation. The interconnects in devices have optimized configurations such as the serpentine, whereby the local strains can be one order of magnitude lower than the applied strain <sup>44, 46</sup>. Therefore, the strain amplitudes involved in the repeated deformations of serpentine interconnects are likely to be small (<5%), which means that the PE874 ink can withstand large numbers of cycles (>1,000) in stretchable applications. The knowledge and characterization of resistance evolution of the ink cycled at small strain amplitudes, gained from this work using straight trace line specimens (and uniform strain distributions), will be used in a future work to model its resistance evolution and fatigue life, including for that of serpentine interconnects upon modeling the local strain distribution of such configurations.

#### 4. CONCLUSIONS

The current work examined the electrical response of the stretchable PE874 conductive ink to uniaxial monotonic and cyclic stretching for different ink geometry (1, 2, and 3 layers, each layer approximately 8-10 µm, and trace widths of 0.5, 1, and 2 mm) and loading conditions. The material

deformation mechanisms responsible for the electrical resistance evolution with monotonic tensile strain and cyclic straining were also investigated. Based on the experimental results, including those of the *in-situ* confocal microscope and SEM experiments, the following conclusions can be drawn.

- 1. Ink geometric conditions, including both ink thickness and trace width, impact the electrical resistance evolution with tensile strain, due to differences in crack pattern resulting from stretching. Narrow trace widths (0.5 mm) are associated with much higher resistance, as cracks traverse the trace width. Thicker inks are associated with higher normalized resistance, in part due to the longer cracks. However, when taking into account the thickness effect on initial resistance, thicker inks provide slightly better resistance under strain.
- 2. For cyclic stretching, there exists a strong correlation between fatigue life  $N_f$ , as defined by the number of cycles until a  $R/R_0$  of 100 is reached, and the strain amplitude  $\epsilon_a$ . The mean strain  $\epsilon_m$  has a secondary effect on  $N_f$ .
- 3. The initial normalized resistance rate  $(R/R_0)'_i$  is found to scale with  $\epsilon_a$ , and is a local maximum value. Therefore this parameter can likely be used to conservatively predict resistance increase for a cyclic test.
- 4. The rate of change in resistance R with cycling, dR/dN (or R'), decreases with ink thickness and trace width for fatigue tests across different strain levels. For practical applications, thicker (≥25 μm) and wider (≥2 mm) inks should be used to lower R increases with repeated deformation.
- 5. During monotonic tensile strain increase, the cracks lengthened as well as widened and deepened; during cyclic stretching between two strain values, the cracks did not lengthen

noticeably but still widened and deepened. Fatigue damage from crack widening and

deepening was found to be responsible for electrical resistance increase during cyclic

stretching to the same strain. The loss of electrical conductivity could be considered to

occur when the crack has effectively deepened to the ink-substrate surface as the crack

faces become completely separated.

ASSOCIATED CONTENT

**Supporting Information** 

This material is available free of charge via the Internet at http://pubs.acs.org.

**AUTHOR INFORMATION** 

**Corresponding Authors** 

E-mail: antonia.antoniou@me.gatech.edu, olivier.pierron@me.gatech.edu

Notes

The authors declare no competing financial interest

**ACKNOWLEDGMENTS** 

The authors gratefully acknowledge funding support from the National Science Foundation (NSF

CMMI-MOMS: 2026936). The authors are grateful to DuPont colleagues (Jeff Meth, Lynne

Dellis and Augustus Jones) for providing samples.

#### **REFERENCES**

- 1. Gao et al., W., Fully integrated wearable sensor arrays for multiplexed in situ perspiration analysis. *Nature* **2016**, *529* (7587), 509-514.
- 2. Imani et al., S., A wearable chemical–electrophysiological hybrid biosensing system for real-time health and fitness monitoring. *Nature communications* **2016**, *7* (1), 1-7.
- 3. Lee et al., H., A graphene-based electrochemical device with thermoresponsive microneedles for diabetes monitoring and therapy. *Nature nanotechnology* **2016**, *11* (6), 566-572.
- 4. Schwartz et al., G., Flexible polymer transistors with high pressure sensitivity for application in electronic skin and health monitoring. *Nature communications* **2013**, *4* (1), 1-8.
- 5. Huang, X.; Liu, Y.; Zhou, J.; Nejad, S. K.; Wong, T. H.; Huang, Y.; Li, H.; Yiu, C. K.; Park, W.; Li, J., Garment embedded sweat-activated batteries in wearable electronics for continuous sweat monitoring. *npj Flexible Electronics* **2022**, *6* (1), 1-8.
- 6. Iqbal, S.; Mahgoub, I.; Du, E.; Leavitt, M. A.; Asghar, W., Advances in healthcare wearable devices. *NPJ Flexible Electronics* **2021**, *5* (1), 1-14.
- 7. Dubal et al., D. P., Towards flexible solid-state supercapacitors for smart and wearable electronics. *Chemical Society Reviews* **2018**, *47* (6), 2065-2129.
- 8. Lv et al., T., Nanocarbon-based materials for flexible all-solid-state supercapacitors. *Advanced Materials* **2018**, *30*, 1-17.
- 9. García Núñez, C.; Manjakkal, L.; Dahiya, R., Energy autonomous electronic skin. *npj Flexible Electronics* **2019**, *3* (1), 1-24.
- 10. Gupta, S.; Navaraj, W. T.; Lorenzelli, L.; Dahiya, R., Ultra-thin chips for high-performance flexible electronics. *npj Flexible Electronics* **2018**, *2* (1), 1-17.
- 11. Kim et al., S., Low-power flexible organic light-emitting diode display device. Advanced Materials. *Advanced Materials* **2011**, *23* (31), 3511-3516.
- 12. Rogers et al., J. A., Paper-like electronic displays: Large-area rubber-stamped plastic sheets of electronics and microencapsulated electrophoretic inks. *Proceedings of the National Academy of Sciences* **2001**, *98* (9), 4835-4840.
- 13. Sekitani et al., T., Stretchable active-matrix organic light-emitting diode display using printable elastic conductors. *Nature materials* **2009**, *8* (6), 494-499.
- 14. Park, Y.; Fuentes-Hernandez, C.; Kim, K.; Chou, W.-F.; Larrain, F. A.; Graham, S.; Pierron, O. N.; Kippelen, B., Skin-like low-noise elastomeric organic photodiodes. *Science Advances* **2021**, *7* (51), eabj6565.
- 15. Chen, Y.; Zhang, Y.; Liang, Z.; Cao, Y.; Han, Z.; Feng, X., Flexible inorganic bioelectronics. *npj Flexible Electronics* **2020**, *4* (1), 1-20.
- 16. Choi, M. K.; Yang, J.; Hyeon, T.; Kim, D.-H., Flexible quantum dot light-emitting diodes for next-generation displays. *npj Flexible Electronics* **2018**, *2* (1), 1-14.
- 17. Kim, S. H.; Song, S. Y.; Kim, S. Y.; Chang, M. W.; Kwon, H. J.; Yoon, K. H.; Sung, W. Y.; Sung, M. M.; Chu, H. Y., A compact polymer–inorganic hybrid gas barrier nanolayer for flexible organic light-emitting diode displays. *npj Flexible Electronics* **2022**, *6* (1), 1-6.

- 18. Hong et al., Y. J., Wearable and implantable devices for cardiovascular healthcare: from monitoring to therapy based on flexible and stretchable electronics. *Advanced Functional Materials* **2019**, *29*, 1-26.
- 19. KIm et al., D., Materials for multifunctional balloon catheters with capabilities in cardiac electrophysiological mapping and ablation therapy. *Nature materials* **2011**, *10* (4), 316-323.
- 20. Chow, J. H.; Sitaraman, S. K.; May, C.; May, J. In *Study of wearables with embedded electronics through experiments and simulations*, 2018 IEEE 68th Electronic Components and Technology Conference (ECTC), IEEE: 2018; pp 814-821.
- 21. Yetisen, A. K.; Martinez-Hurtado, J. L.; Ünal, B.; Khademhosseini, A.; Butt, H., Wearables in medicine. *Advanced Materials* **2018**, *30* (33), 1706910.
- 22. Hommel, M.; Kraft, O., Deformation behavior of thin copper films on deformable substrates. *Acta Materialia* **2001**, *49* (19), 3935-3947.
- 23. Kraft, O.; Hommel, M.; Arzt, E., X-ray diffraction as a tool to study the mechanical behaviour of thin films. *Materials Science and Engineering* **2000**, *288* (2), 209-216.
- 24. Lacour, S. P.; Wagner, S.; Huang, Z.; Suo, Z., Stretchable gold conductors on elastomeric substrates. *Applied physics letters* **2003**, *82* (15), 2404-2406.
- 25. Lambricht, N.; Pardoen, T.; Yunus, S., Giant stretchability of thin gold films on rough elastomeric substrates. *Acta materialia* **2013**, *61* (2), 540-547.
- 26. Niu, R. M.; Liu, G.; Wang, C.; Zhang, G.; Ding, X. D.; Sun, J., Thickness dependent critical strain in submicron Cu films adherent to polymer substrate. *Applied Physics Letters* **2007**, *90* (16).
- 27. Xiang, Y.; Li, T.; Suo, Z.; Vlassak, J. J., High ductility of a metal film adherent on a polymer substrate. *Applied Physics Letters* **2005**, *87* (16).
- 28. Yu, D. Y.; Spaepen, F., The yield strength of thin copper films on Kapton. *Journal of Applied Physics* **2004**, *95* (6), 2991-2997.
- 29. Cordill, M. J.; Kreiml, P.; Mitterer, C., Materials Engineering for Flexible Metallic Thin Film Applications. *Materials* **2022**, *15* (3), 926.
- 30. Kaiser, T.; Cordill, M.; Kirchlechner, C.; Menzel, A., Electrical and mechanical behaviour of metal thin films with deformation-induced cracks predicted by computational homogenisation. *International Journal of Fracture* **2021**, *231* (2), 223-242.
- 31. Sim, G.-D.; Lee, Y.-S.; Lee, S.-B.; Vlassak, J. J., Effects of stretching and cycling on the fatigue behavior of polymer-supported Ag thin films. *Materials Science and Engineering: A* **2013**, *575*, 86-93.
- 32. Sim, G.-D.; Hwangbo, Y.; Kim, H.-H.; Lee, S.-B.; Vlassak, J. J., Fatigue of polymer-supported Ag thin films. *Scripta Materialia* **2012**, *66* (11), 915-918.
- 33. Glushko, O.; Cordill, M., In-operando fatigue behavior of gold metallization lines on polyimide substrate. *Scripta Materialia* **2020**, *186*, 48-51.
- 34. Cahn, G.; Barrios, A.; Graham, S.; Meth, J.; Antoniou, A.; Pierron, O., The role of strain localization on the electrical behavior of flexible and stretchable screen printed silver inks on polymer substrates. *Materialia* **2020**, *10*, 100642.
- 35. Merilampi, S.; Laine-Ma, T.; Ruuskanen, P., The characterization of electrically conductive silver ink patterns on flexible substrates. *Microelectronics reliability* **2009**, *49* (7), 782-790.
- 36. Shin, D.-Y.; Lee, Y.; Kim, C. H., Performance characterization of screen printed radio frequency identification antennas with silver nanopaste. *Thin Solid Films* **2009**, *517* (21), 6112-6118.
- 37. Kim, S.; Sung, H. J., Effect of printing parameters on gravure patterning with conductive silver ink. *Journal of Micromechanics and Microengineering* **2015**, *25* (4).
- 38. Sung, D.; de la Fuente Vornbrock, A.; Subramanian, V., Scaling and optimization of gravure-printed silver nanoparticle lines for printed electronics. *IEEE Transactions on Components and Packaging Technologies* **2009**, *33* (1), 105-114.

- 39. Borghetti, M.; Serpelloni, M.; Sardini, E.; Pandini, S., Mechanical behavior of strain sensors based on PEDOT: PSS and silver nanoparticles inks deposited on polymer substrate by inkjet printing. *Sensors and Actuators A: Physical* **2016**, *243*, 71-80.
- 40. Schlisske, S.; Raths, S.; Ruiz-Preciado, L. A.; Lemmer, U.; Exner, K.; Hernandez-Sosa, G., Surface energy patterning for ink-independent process optimization of inkjet-printed electronics. *Flexible and Printed Electronics* **2021**, *6* (1), 015002.
- 41. Tafoya, R. R.; Secor, E. B., Understanding effects of printhead geometry in aerosol jet printing. *Flexible and Printed Electronics* **2020**, *5* (3), 035004.
- 42. Van Osch, T. H.; Perelaer, J.; De Laat, A. W.; Schubert, U. S., Inkjet printing of narrow conductive tracks on untreated polymeric substrates. *Advanced Materials* **2008**, *20* (2), 343-345.
- 43. Yang, W.; Mathies, F.; Unger, E. L.; Hermerschmidt, F.; List-Kratochvil, E. J., One-pot synthesis of a stable and cost-effective silver particle-free ink for inkjet-printed flexible electronics. *Journal of Materials Chemistry C* **2020**, *8* (46), 16443-16451.
- 44. Koshi, T.; Nomura, K.-i.; Yoshida, M., Measurement and analysis on failure lifetime of serpentine interconnects for e-textiles under cyclic large deformation. *Flexible and Printed Electronics* **2021**, *6* (2), 025003.
- 45. Sliz, R.; Huttunen, O.-H.; Jansson, E.; Kemppainen, J.; Schroderus, J.; Kurkinen, M.; Fabritius, T., Reliability of R2R-printed, flexible electrodes for e-clothing applications. *npj Flexible Electronics* **2020**, *4* (1), 1-9.
- 46. Zhang, Y.; Xu, S.; Fu, H.; Lee, J.; Su, J.; Hwang, K.-C.; Rogers, J. A.; Huang, Y., Buckling in serpentine microstructures and applications in elastomer-supported ultra-stretchable electronics with high areal coverage. *Soft Matter* **2013**, *9* (33), 8062-8070.
- 47. Cahn, G.; Pierron, O.; Antoniou, A., Electrical performance evolution and fatigue mechanisms of silver-filled polymer ink under uniaxial cyclic stretch. *Flexible and Printed Electronics* **2021**, *6* (3), 035008.
- 48. Cahn, G.; Pierron, O.; Antoniou, A., Trace width effects on electrical performance of screen-printed silver inks on elastomeric substrates under uniaxial stretch. *Journal of Applied Physics* **2021**, *130* (11), 115304.
- 49. Blaber, J.; Adair, B.; Antoniou, A., Ncorr: open-source 2D digital image correlation matlab software. *Experimental Mechanics* **2015**, *55* (6), 1105-1122.
- 50. Hutchinson, J. W.; Suo, Z., Mixed mode cracking in layered materials. *Advances in applied mechanics* **1991**, *29*, 63-191.
- 51. Ye, T.; Suo, Z.; Evans, A., Thin film cracking and the roles of substrate and interface. *International Journal of Solids and Structures* **1992**, *29* (21), 2639-2648.
- 52. Vlassak, J. J., Channel cracking in thin films on substrates of finite thickness. *International Journal of Fracture* **2003**, *119* (4), 299-323.
- 53. Glushko, O.; Kraker, P.; Cordill, M., Explicit relationship between electrical and topological degradation of polymer-supported metal films subjected to mechanical loading. *Applied Physics Letters* **2017**, *110* (19), 191904.
- 54. Gebhart, D. D.; Krapf, A.; Gammer, C.; Merle, B.; Cordill, M. J., Linking through-thickness cracks in metallic thin films to in-situ electrical resistance peak broadening. *Scripta Materialia* **2022**, *212*, 114550.